

# Scalable Multi-Task Learning for Particle Collision Event Reconstruction with Heterogeneous Graph Neural Networks

William Sutcliffe<sup>1</sup>, Marta Calvi<sup>2,3</sup>, Simone Capelli<sup>3</sup>, Jonas Eschle<sup>5</sup>, Julián García Pardiñas<sup>4</sup>, Abhijit Mathad<sup>5</sup>, Azusa Uzuki<sup>1</sup> and Nicola Serra<sup>1</sup>

<sup>1</sup> Department of Physics, University of Zürich, Winterthurerstrasse 190, Zürich, 8057, Switzerland.

<sup>2</sup> Dipartimento di Fisica “G. Occhialini”, Università di Milano Bicocca, Piazza della Scienza 3, Milano, 20126, Italy

<sup>3</sup> INFN Sezione di Milano-Bicocca, Piazza della Scienza 3, Milano, 20126, Italy

<sup>4</sup> Laboratory for Nuclear Science. Massachusetts Institute of Technology (MIT), 77 Massachusetts Ave, Cambridge, MA 02139, USA.

<sup>5</sup> Experimental Physics Department, European Organization for Nuclear Research (CERN), Espl. des Particules 1, Meyrin, 1211, Switzerland.

E-mail: [william.sutcliffe@cern.ch](mailto:william.sutcliffe@cern.ch)

**Abstract.** The growing luminosity frontier at the Large Hadron Collider is challenging the reconstruction and analysis of particle collision events. Increased particle multiplicities are straining latency and storage requirements at the data acquisition stage, while new complications are emerging, including higher background levels and more frequent particle vertex misassociations. This in turn necessitates the development of more holistic and scalable reconstruction methods that take advantage of recent advances in machine learning. We propose a novel Heterogeneous Graph Neural Network (HGNN) architecture featuring unique representations for diverse particle collision relationships and integrated graph pruning layers for scalability. Trained with a multi-task paradigm in an environment mimicking the LHCb experiment, this HGNN significantly improves beauty hadron reconstruction performance. Notably, it concurrently performs particle vertex association and graph pruning within a single framework. We quantify reconstruction and pruning performance, demonstrate enhanced inference time scaling with event complexity, and mitigate potential performance loss using a weighted message passing scheme.

## 1. Introduction

Over the past two decades, the field of neural networks has witnessed rapid advancements, driving breakthroughs across diverse domains such as natural language processing, image analysis, and scientific computation. Architectures ranging from convolutional neural networks [1] to the more recent transformer [2] models have played pivotal roles in these developments. Meanwhile, graph neural networks [3] (GNNs) have emerged as a powerful tool for representing complex datasets of variable-size that lack explicit spatial or sequential structures, effectively modeling interactions among multiple entities and their interconnections.

Building on this success, heterogeneous GNNs [4] (HGNNs) extend conventional GNNs by incorporating multiple types of nodes and edges, enabling richer and more context-specific representations for complex, multi-relational data. HGNNs find extensive application in areas such as recommendation systems (modeling users, items, and interactions) [5], bioinformatics (gene-disease-drug networks) [6], and natural language processing tasks like cross-lingual text classification [7].

In parallel, multi-task learning has gained traction as an approach that simultaneously optimises several related objectives, allowing models to share representations and improve generalization across tasks [8]. By leveraging the synergies among tasks, multi-objective learning can not only enhance performance but also provide a more holistic understanding of underlying data representations.

Concurrently, in particle physics recent trends have shown a rising employment of machine learning (ML) across several domains including simulation, detector reconstruction and particle classification [9, 10]. HGNNs and multi-task learning are particularly applicable at particle collider experiments given that particle collision events are inherently heterogeneous involving several object types and their relationships with one another. However, despite their potential, HGNNs have rarely been applied in particle physics, where most applications of GNNs rely on homogeneous GNN architectures [11–13]. Unifying HGNNs and multi-task learning allows for several reconstruction tasks in parallel.

The LHCb experiment [14] at CERN’s Large Hadron Collider focuses on high-precision studies of beauty ( $b$ ) and charm ( $c$ ) quarks. Its main goals are to test the Standard Model (SM) through measurements of CP violation, rare beauty hadron decays, and flavor-changing neutral current processes that are highly sensitive to new physics beyond the SM. During Runs 1 and 2 (2010-2018), LHCb recorded  $9\text{ fb}^{-1}$  of proton-proton collision data at a luminosity of  $4 \times 10^{32}\text{ cm}^{-2}\text{ s}^{-1}$ . A recent upgrade (Upgrade I) for Runs 3 and 4 increased the luminosity to  $2 \times 10^{33}\text{ cm}^{-2}\text{ s}^{-1}$ , resulting in an average of 5 collisions per event and a charged particle track multiplicity of around 150 [15]. Looking ahead, Upgrade II at the High-Luminosity LHC is expected to boost the luminosity tenfold, yielding roughly 50 collisions per event [16] and a track multiplicity of around 1,000 particles.

The rising collision event complexity at the LHCb experiment presents significant challenges for data acquisition and measurement precision. While LHCb’s Upgrade I trigger framework [17] already transitioned to partial event storage, moving beyond the traditional approach of storing full events which was feasible when disk space was less constrained [18], the challenges intensify under HL-LHC conditions. The anticipated increase in particle multiplicity and the common occurrence of multiple heavy-hadron decays within single events will further strain storage resources. Consequently, refining strategies to systematically identify and preserve the most valuable event components remains an important objective, especially considering the diverse heavy-hadron species and decays per species, whose combinatorics raise to tens of thousands of different possible decays of interest. While exclusive selections are advantageous for storage and crucial for many physics analyses to avoid biases, capturing sufficient information for studies requiring context from the underlying event (e.g., for flavour tagging or semileptonic decay spectroscopy) presents an ongoing challenge. Developing techniques that can selectively preserve this broader event information, when needed for specific physics goals, while adhering to stringent latency constraints ( $\mathcal{O}(100\text{ms})$  per event) and storage

limitations ( $\mathcal{O}(10\text{PB})$  per year), will be beneficial for maximising the physics potential.

Another critical issue emerging in the context of increased luminosity conditions at LHCb is primary vertex (PV) misassociation. PVs correspond to the proton-proton interaction points, and under high-luminosity conditions, multiple such interactions can occur in a single event. Misassociation arises when tracks or decay products from overlapping proton-proton collisions are incorrectly attributed to the wrong PV. This can severely degrade vertex resolution and bias the measurement of key observables, such as the  $B$ -hadron decay flight distance and direction, ultimately affecting the precision of determinations of time-dependent CP violation [19] and measurements of decays with missing energy [20, 21]. Addressing PV misassociation is therefore paramount to maintaining the high-precision performance required for LHCb’s physics program in the high-luminosity era, prompting the need for innovative reconstruction algorithms and advanced machine learning techniques.

Recently, we proposed the Deep Full Event Interpretation (DFEI) algorithm [22], employing GNNs to perform a multi-stage inclusive reconstruction of beauty hadrons in LHCb collision events. Despite its potential, the computational cost and scalability of its multi-stage approach pose significant challenges with regards to meeting the low-latency requirements of a real-time trigger environment. Furthermore, the algorithm does not address the pressing issue of PV misassociation. Building upon the success of our earlier work, we propose a HGNN architecture with integrated graph pruning for scalability, which is trained with multiple objectives to perform beauty hadron reconstruction and PV association within a unified framework.

## 2. Related work

Particle decay reconstruction typically follows an exclusive strategy, in which final-state particles are successively combined into intermediate structures to form complete decay chains for specific topologies. This process proceeds sequentially, combining final-state particles into higher-level structures based on predefined decay modes and kinematic constraints, such as invariant mass thresholds or conservation of momentum and energy. At each level, particle identification techniques and machine learning classification algorithms may be applied to improve the reconstruction accuracy and resolve ambiguities.

Beyond traditional methods that target individual decay channels, intermediate strategies exist that bridge these and the fully holistic reconstruction we propose. Key examples include the LHCb topological trigger [23, 24] and the Belle II tag-side reconstruction algorithm known as the Full Event Interpretation (FEI) [25]. The LHCb topological trigger identifies beauty hadron decays based on predefined characteristic topologies, which rely on multivariate classifiers trained on an ensemble of decay modes making its selection inherently guided by predefined exclusive states. Similarly, the FEI performs a hierarchical reconstruction of a large number of beauty decay chains with a dedicated multivariate classifier for each unique particle decay.

More recently, there have been several efforts towards a fully inclusive reconstruction of beauty hadron decays with GNNs at LHCb and Belle II [22, 26, 27]. These developments were prompted by Kahn *et al.* [26] with the introduction of a novel edge classification target for hierarchical decay chains known as the Lowest Common Ancestor Generations (LCAG) matrix. This compact representation enables one to learn the hierarchical structure of a decay solely

from its final-state particles. For each edge relation between final-state particles a multi-class label is used, which signifies the generational class of the shared ancestor.

Our previous publication [22], the Deep Full Event Interpretation (DFEI), expanded on this work demonstrating the inclusive reconstruction of beauty hadron decays with GNNs within the hadronic environment of LHCb, which is complicated by a large number of background particles. To overcome these difficulties, we employed a multi-stage approach. First, a node-pruning GNN filters out background nodes based on kinematic and topological features. Next, an edge-pruning GNN removes unlikely associations, simplifying the event graph. Lastly, a final GNN processes the remaining graph and performs the edge classification of LCAG values between nodes, enabling a separation and hierarchical reconstruction of multiple possible beauty hadron decay chains in each event.

Beyond particle decay reconstruction, GNNs have seen significant adoption in particle physics [11]. For charged particle tracking, GNNs are employed to connect detector hits (nodes) into particle trajectories by classifying potential track segments (edges) [28]. GNNs have demonstrated an improved performance for flavor tagging of beauty hadron events at Belle II with GFlaT [29]. GNNs are also increasingly used for jet classification and reconstruction tasks, representing jets as point clouds or graphs of constituent particles to distinguish between different originating particles and better reconstruct the kinematical quantities of the jet [30–32]. Furthermore, GNNs are employed for particle flow (PF) algorithms, aiming to provide an end-to-end ML approach that combines information from different subdetectors to reconstruct a complete list of particles [33]. While most applications use homogeneous GNNs, HGNNs have been applied to improve hadronic  $\tau$  lepton identification by treating tracks and energy clusters as distinct node types within a jet graph [12] and in novel designs for track reconstruction that explicitly account for different detector sensor types (e.g., pixel vs. strip hits) [13].

To manage computational costs and focus on relevant relations, two main strategies are employed: graph pruning and dynamic graph construction. Graph pruning typically starts with a larger, often geometrically constrained graph, and then removes edges deemed unlikely to represent true physical connections. This is common in tracking pipelines (e.g. ExaTrkX), where initial filtering steps or GNN-based edge classifiers prune the graph significantly before track finding [34, 35]. Usually thresholding the output scores of edge-classifying GNNs serves as the pruning mechanism. Alternatively, dynamic graph construction methods adapt the graph connectivity during the learning process. Techniques like k-Nearest Neighbors (k-NN) applied in a learned latent space allow the graph structure to evolve, connecting nodes based on their learned features rather than just initial geometry. This is exemplified by architectures like EdgeConv (used in ParticleNet for jet tagging) [30] and GravNet (used for calorimeter clustering) [36], which dynamically define edges. Both pruning and dynamic construction aim to improve the overall performance and scalability of GNNs.

Lastly, multi-task learning (MTL), the paradigm we adopt, has become increasingly relevant in particle physics, where complex analysis often involves inferring multiple correlated properties or performing hierarchical reconstruction steps. For instance, in jet physics, “foundation models” are being developed using MTL principles, pre-training on large datasets for self-supervised tasks like jet generation or masked particle prediction, then fine-tuning for various downstream tasks like jet tagging or property prediction, aiming to create a universal jet representation [37–39]. In neutrino physics event reconstruction, MTL is used in GNNs

like NuGraph2 to simultaneously perform tasks such as detector hit classification and semantic segmentation (assigning hits to particle types like electron or muon) [40]. The concept also extends to using auxiliary tasks to aid a primary goal, such as predicting track origins alongside flavour tagging in ATLAS’s GNN jet tagger (GN1) [31]. Beyond particle physics, MTL is also used in related fields such as fusion energy for real-time plasma equilibrium reconstruction, simultaneously predicting multiple plasma parameters and profile distributions [41].

### 3. Methodology

#### 3.1. Graph Neural Networks

GNNs encompass a diverse range of architectures, each tailored to specific tasks and graph structures. Key approaches include Graph Convolutional Networks (GCNs) [42], which extend traditional convolutions by aggregating and transforming features from connected nodes, and Graph Attention Networks (GATs) [43], which use attention mechanisms to weight node contributions. Message Passing Neural Networks (MPNNs) [44] further unify these methods under a general framework where interconnected nodes iteratively exchange and update messages to learn graph representations.

In this paper we build upon the GNN introduced by Battaglia *et al.* [45], which provides a more comprehensive and versatile framework for MPNNs learning representations at multiple levels, including nodes, edges, and globally, making it well-suited to capture the hierarchical and relational information inherent in particle collisions. Equation 1 summarises the update equations for the GNN, which consist of edge, node and graph updates.

$$\begin{aligned} e'^k &= \phi^e(e^k, v^{r_k}, v^{s_k}, u) & \bar{e}'^i &= \rho^{e \rightarrow v}(\{E'^i\}) \\ v'^i &= \phi^v(\bar{e}'^i, v^i, u) & \bar{e}' &= \rho^{e \rightarrow u}(\{E'\}) \\ u' &= \phi^u(\bar{e}', \bar{v}', u) & \bar{v}' &= \rho^{v \rightarrow u}(\{V'\}) \end{aligned} \quad (1)$$

The edge update function  $\phi^e$  is a learnable Multi-Layer-Perceptron (MLP), which takes as input the existing edge representation  $e^k$  for edge  $k$ , adjoining receiver and sender node representations ( $v^{r_k}$  and  $v^{s_k}$ ) and a global representation  $u$ . The subsequent node update with MLP  $\phi^v$  for node  $i$ , takes as input the node  $v^i$  representation, the edge to node aggregation  $\bar{e}'^i$  and  $u$ . With  $\bar{e}'^i$  aggregating edge representations for the set of edges  $E'^i$  that node  $i$  receives using a aggregation function  $\rho^{e \rightarrow v}$ . Lastly, sets of edges and nodes,  $E'$  and  $V'$ , are aggregated globally yielding,  $\bar{e}'$  and  $\bar{v}'$ , using aggregation functions  $\rho^{e \rightarrow u}$  and  $\rho^{v \rightarrow u}$ . The global update  $u'$  with MLP  $\phi^u$  takes as input the global aggregations and the existing global representation,  $u$ .

#### 3.2. HGNN layer for particle reconstruction and pruning

HGNNs improve upon homogeneous GNNs by natively handling multiple node and edge types with type-specific representations and update functions, unlike the uniform approach of homogeneous GNNs. This inherent flexibility makes HGNNs better suited for modeling diverse systems, like physical interactions. While homogeneous GNNs can mimic this heterogeneity using techniques like one-hot encoding and padding, they lack the inherent inductive bias of HGNNs, often leading to suboptimal representations and making it difficult to set distinct learning objectives for different entity types.

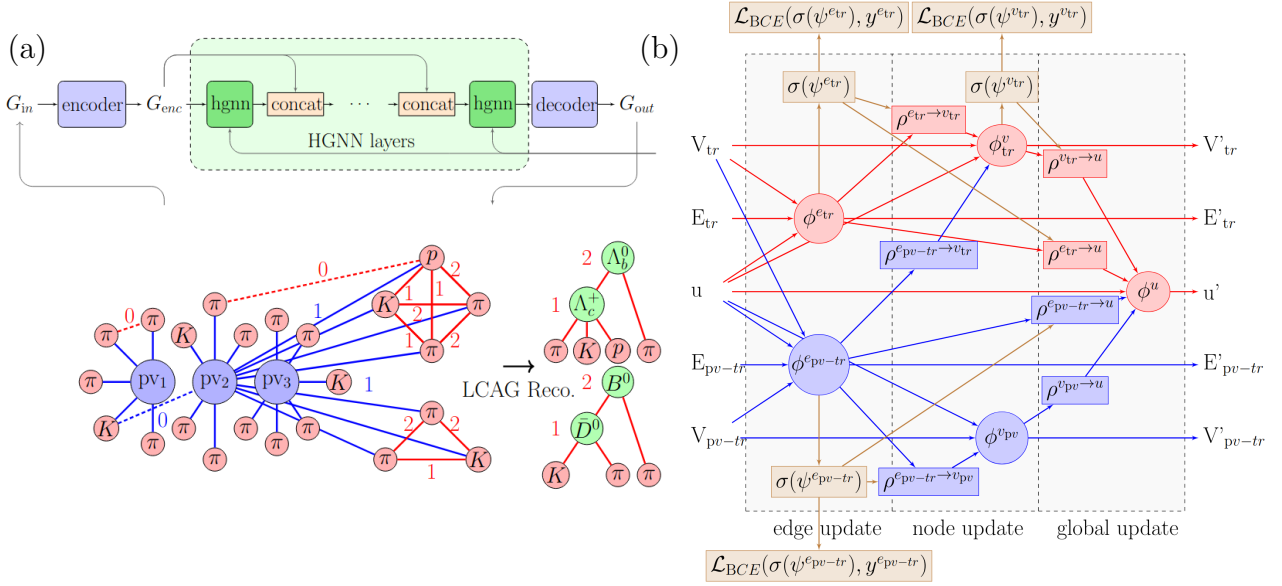


**Figure 1.** (a) Heterogeneous graph representation (below) and HGNN architecture (above) for a simultaneous beauty hadron reconstruction and PV association. In the graph solid lines indicate all true edges and their class labels, while dotted lines provide examples of false edges with label zero. (b) Heterogeneous modification in blue to the GNN layer updates from Battaglia *et al.* [45] in red. The addition of pruning tasks is shown in light brown.

Figure 1(a) illustrates the heterogeneous nature of a LHCb collision event with multiple reconstructed PVs, which produce  $\mathcal{O}(100-1,000)$  charged particle tracks. Data relations within the collision event can be naturally represented by a heterogeneous graph, with PV and track node types, and track-track and PV-track edges, which signify relations between the various node objects. Here, we chose not to include PV-PV edges as they are not directly associated with any learning objective. Our previous DFEI algorithm assigned each track to a PV with a minimum impact parameter and appended the corresponding PV’s coordinates as static track-node features. This both capped performance, since the model couldn’t learn to select the correct PV dynamically, and increased memory requirements by duplicating the same coordinates across tracks. In contrast, a heterogeneous graph explicitly encodes PV-track edges, allowing the end-to-end learning of associations and eliminating repetitions of PV data.

To enable learning graph representations for joint beauty hadron reconstruction and PV association, we propose a heterogeneous extension of the GNN layer of Battaglia *et al.*. We denote track and PV node representations,  $v_{tr}^i$  and  $v_{pv}^j$ , track-track and PV-track edge representations,  $e_{tr}^k$  and  $e_{pv-tr}^l$ . The corresponding edge, node and global representation updates for our HGNN layer are,

$$\begin{aligned}
 e_{tr}^k &= \phi^{e_{tr}}(e_{tr}^k, v_{tr}^k, v_{tr}^s, u) & \bar{e}_{tr}^i &= \rho^{e_{tr} \rightarrow v_{tr}}(\{E_{tr}^i\}) \\
 e_{pv-tr}^l &= \phi^{e_{pv-tr}}(e_{pv-tr}^l, v_{tr}^l, v_{pv}^l, u) & \bar{e}_{pv-tr}^i &= \rho^{e_{pv-tr} \rightarrow v_{tr}}(\{E_{pv-tr}^i\}) \\
 v_{tr}^i &= \phi^{v_{tr}}(v_{tr}^i, \bar{e}_{tr}^i, \bar{e}_{pv-tr}^i, u) & \bar{e}_{pv-tr}^j &= \rho^{e_{pv-tr} \rightarrow v_{pv}}(\{E_{pv-tr}^j\}) \\
 v_{pv}^j &= \phi^{v_{pv}}(v_{pv}^j, \bar{e}_{pv-tr}^j, u) & \bar{e}_{tr} &= \rho^{e_{tr} \rightarrow u}(\{E_{tr}'\}), \bar{v}_{tr}' = \rho^{v_{tr} \rightarrow u}(\{V_{tr}'\}) \\
 u' &= \phi^u(\bar{e}_{tr}', \bar{e}_{pv-tr}', \bar{v}_{tr}', \bar{v}_{pv}', u) & \bar{e}_{tr-pv}' &= \rho^{e_{tr-pv} \rightarrow u}(\{E_{tr-pv}'\}), \bar{v}_{pv}' = \rho^{v_{pv} \rightarrow u}(\{V_{pv}'\}) ,
 \end{aligned} \tag{2}$$

where the HGNN layer update begins with edge updates,  $e_{tr}^k$  and  $e_{pv-tr}^l$ , applying MLPs  $\phi^{e_{tr}}$

and  $\phi^{e_{\text{pv-tr}}}$ . Meanwhile, node updates,  $v_{\text{tr}}^i$  and  $v_{\text{pv}}^j$  with MLPs  $\phi^{v_{\text{tr}}}$  and  $\phi^{v_{\text{pv}}}$  subsequently take as input aggregated edge representations for multiple edge types. The inputs of the  $v_{\text{tr}}^i$  update includes the aggregated track edges  $\bar{e}_{\text{tr}}^i$  and PV-track edges  $\bar{e}_{\text{pv-tr}}^i$ . Meanwhile, the update  $v_{\text{pv}}^j$  includes the aggregation of PV-track edges to PV nodes,  $\bar{e}_{\text{pv-tr}}^j$ . Lastly, the global update uses as input aggregations of all node and edge types globally,  $\bar{e}_{\text{tr}}'$ ,  $\bar{e}_{\text{pv-tr}}'$ ,  $\bar{v}_{\text{tr}}'$ ,  $\bar{v}_{\text{pv}}'$ . Figure 1(b), demonstrates the various HGNN layer computations of equation 2 for node and edge inputs from tracks (red) and PVs (blue).

To enhance the scalability of the HGNN in potential real-time data acquisition settings, we incorporate edge and node pruning directly into its layers. The goal is to learn node and edge scores that can be used to remove irrelevant nodes and edges at inference time. To this end, we introduce node and edge scores,  $\hat{y}^v = \sigma(\psi^v(v'))$  and  $\hat{y}^e = \sigma(\psi^e(e'))$ , where  $\psi^v$  and  $\psi^e$  are MLPs operating on the updated node and edge representations  $v'$  and  $e'$  from Equation 2, and  $\sigma$  denotes the Sigmoid function. These probability scores can be trained in two ways: using a Binary Cross-Entropy loss  $\mathcal{L}_{\text{BCE}}(\hat{y}^{v/e}, y^{v/e})$  when domain knowledge provides suitable ground-truth pruning labels  $y^v$  and  $y^e$ , or implicitly, by using the predicted scores  $\hat{y}^v$  and  $\hat{y}^e$  as weights within the HGNN aggregation functions. We explore both approaches in our ablation studies in Section 4.1.

Pruning can be performed either via a top- $k$  operation or by introducing a threshold  $y_{\text{cut}}$ . In this paper, we adopt the latter approach given better observed performance and greater interpretability in terms of purity. Furthermore, we focus on the application of pruning during inference to boost speed and remove redundant background edges and nodes to enhance reconstruction performance. We acknowledge that integrating pruning into training (i.e., ‘pruning-aware’ training, a form of dynamic graph construction) could further improve reconstruction. Despite not employing pruning-aware training, our empirical results show that incorporating extra MLPs per node and edge improves the algorithm’s performance, as detailed in subsequent sections.

### 3.3. HGNN architecture and objective loss

The full HGNN architecture is shown in Figure 1(a), which processes as input  $G_{\text{in}}$  including track and PV node and edge input features through an encoder layer, several HGNN layers with integrated graph pruning and finally a decoder layer resulting in  $G_{\text{out}}$ . The encoder and decoder layers consist of MLP node, edge and global updates,  $\chi(v)$ ,  $\chi(e)$  and  $\chi(u)$ . The encoded graph representation,  $G_{\text{enc}}$ , is concatenated with the output graph representation from each HGNN layer to preserve important information from the input features and prevent oversmoothing [46]. Hyperparameters of the HGNN include the number of HGNN layers ( $n_{\text{layers}}^{\text{HGNN}} = 8$ ) and layers within MLPs ( $n_{\text{layers}}^{\text{MLP}} = 4$ ), the MLP hidden channel dimensions ( $d_{\text{h}}^{\chi} = d_{\text{h}}^{\phi} = 128$  and  $d_{\text{h}}^{\psi} = 16$ ) and the MLP output dimensions ( $d_{\text{h}}^{\chi} = d_{\text{h}}^{\phi} = 16$  and  $d_{\text{h}}^{\psi} = 1$ ). All MLPs employ ReLU activation functions and batch norm, meanwhile aggregation functions use summation. The hyperparameters were chosen on the basis of an observed saturation in the validation loss with model complexity.

The HGNN is trained to accomplish beauty hadron reconstruction, graph pruning and PV

association tasks by minimising a multi-objective loss,

$$\begin{aligned} \mathcal{L} = & \mathcal{L}_{\text{CE}}(e_{\text{out}}, y^{\text{LCA}}) + \beta^{e_{\text{tr}}} \sum_i^{n_{\text{layers}}^{\text{GNN}}} \mathcal{L}_{\text{BCE}}(\hat{y}_i^{e_{\text{tr}}}, y_i^{e_{\text{tr}}}) + \beta^{v_{\text{tr}}} \sum_i^{n_{\text{layers}}^{\text{GNN}}} \mathcal{L}_{\text{BCE}}(\hat{y}_i^{v_{\text{tr}}}, y_i^{v_{\text{tr}}}) \\ & + \beta^{e_{\text{pv-tr}}} \sum_i^{n_{\text{layers}}^{\text{GNN}}} \mathcal{L}_{\text{BCE}}(\hat{y}_i^{e_{\text{pv-tr}}}, y_i^{e_{\text{pv-tr}}}) \end{aligned} \quad (3)$$

where in the first term  $\mathcal{L}_{\text{CE}}$  denotes a class weighted cross-entropy loss,  $e_{\text{out}}$  is the output HGNN edge representation and  $y^{\text{LCA}}$  is a multi-class target for the LCA reconstruction task. The subsequent terms represent the edge and node pruning tasks introduced in Section 3.2, where the significance of the corresponding pruning task relative to the LCA task is scaled with  $\beta$  parameters. The pv-tr edge pruning task effectively performs a PV association by selecting the pv-tr edge with the highest probability score  $\hat{y}^{e_{\text{pv-tr}}}$  for a given track. By default trainings used  $\beta^{e_{\text{tr}}} = 30$ ,  $\beta^{v_{\text{tr}}} = 3$  and  $\beta^{e_{\text{pv-tr}}} = 1$ , which were not optimal, therefore the sensitivity of the multi-objective optimisation to these parameters is further investigated in Appendix B.

We benchmark the HGNN architecture against a GNN, using GNN layer updates according to equation 1, and an equivalent pruning mechanism. The GNN only considers tracks and their interconnections as nodes and edges, respectively. Meanwhile, it uses the same objective loss and hyperparameter values but with the removal of the pv-tr edge pruning task. For both GNN and HGNN architectures, we also quantify the inclusion of weighted aggregations during message passing and denote the corresponding architectures as WGNN and WHGNN.

### 3.4. Datasets and training procedure

The model is trained, validated and tested with the publicly available datasets from our previous publication DFEI [47]. The datasets were produced with a custom simulation environment using PYTHIA8 [48] and EvtGen [49] to simulate particle collision conditions anticipated for LHCb Run 3. Only events containing at least one beauty hadron are considered; these hadrons are then decayed with EvtGen into a variety of known modes. All results in this paper focus exclusively on charged particles produced within the LHCb geometrical acceptance and the Vertex Locator region. Particles outside these regions and neutral particles are not considered, meaning that they are also excluded from the ground truth heavy-hadron decay chains. Additional exclusive datasets, in which one of the beauty hadrons are required to decay to several exclusive decays, are used to further evaluate the model performance.

As depicted in Figure 1, the collision events are represented as a heterogeneous graph. Each node and edge type has an input feature representation. For charged particles (tracks), the input feature representations include the track origin point,  $(x_{\text{tr}}, y_{\text{tr}}, z_{\text{tr}})$ , the track momenta  $(p_x, p_y, p_z)$  and track charge  $q$ . Meanwhile, PV nodes are represented by their position coordinate,  $(x_{\text{pv}}, y_{\text{pv}}, z_{\text{pv}})$ . In contrast, for GNN benchmarks, we adopt the DFEI's approach of appending the coordinates of the PV with minimum impact parameter to the features of each track. Although highly discriminating timing information is anticipated for PV association in LHCb Upgrade II, this study limits its scope to using only these defined positional and kinematic features.



Initially, a fully connected graph is defined between all track and PV nodes with track-track and track-PV edges. The input edge representation for PV-track edges includes solely the impact parameter of the track with respect to the PV. Meanwhile, for track-track edges features, include the angle  $\theta$  between the three-momentum directions of the two particles, the difference  $\Delta z_{\text{tr}}$  in origin  $z_{\text{tr}}$ , a boolean indicating a shared PV according to minimum impact parameter and the momentum-transverse distance, which is the distance between the origin points in a plane transverse to the momentum direction. We adopted a loose prefiltering of track-track edges with 99% efficiency from the DFEI [22], which requires edges to satisfy  $\theta < 0.26$  rad. or the condition of a shared PV according to minimum impact parameter. For the remaining edges, the LCAG ground-truth is determined  $y^{\text{LCA}}$ , where  $y^{\text{LCA}} = 0$  indicates no shared ancestors. The non-zero values are restricted to  $y^{\text{LCA}} = 1, 2, 3$ , which were found to be sufficient to represent the decay hierarchies present in the simulation dataset.

The training and validation datasets consist of 40,000 and 10,000 events respectively, which are equivalent to those used in our previous work. Nominal training for the ablation studies was carried out on an NVIDIA L40S GPU with a batch size of 12. For ablation studies, a base schedule consisted of 30 epochs at a learning rate of  $\alpha = 10^{-3}$ , followed by two epochs at  $\alpha = 10^{-4}$ . Before evaluating the reconstruction performance of selected architectures, we fine-tuned with two additional epochs at  $\alpha = 5 \times 10^{-5}$  and two at  $\alpha = 2 \times 10^{-5}$ . During all training phases, training and validation losses as well as classification accuracies were monitored (see Appendix A for training and validation loss curves). The final performance was measured on a test set of 10,000 independent inclusive beauty-hadron decay events and on multiple exclusive decay datasets, each containing 5,000 events.

## 4. Results

### 4.1. Ablation studies

To quantify the relative merits of the novel architectural developments, several ablation models were trained under similar conditions as described in Section 3.4. Model architectures are either GNN or HGNN and W signifies the use of the weighted message passing introduced in Section 3.2. Ablations further quantify the addition or removal of track node and edge pruning ( $\mathcal{L}_{\text{BCE}}^{\text{prune}}$ ) and PV association ( $\mathcal{L}_{\text{BCE}}^{\text{PV}}$ ) tasks by removing the corresponding BCE loss terms from equation 3 during training.

Table 1 shows the various performance metrics including the LCAG loss  $\mathcal{L}_{\text{CE}}^{\text{LCA}}$  and class accuracies as evaluated with the test dataset. Incorporating additional simultaneous tasks consistently improves the accuracy of LCAG reconstruction with the largest gains seen when including track edge and node pruning tasks, which also serve the primary motivation of accelerating inference time as demonstrated in Section 4.2. Although, GNN and HGNN architectures achieve comparable LCAG reconstruction performance, only the HGNN supports PV association, the results of which are presented in Section 4.4. Based on the ablation studies we only present subsequent performance results for GNN and HGNN architectures trained with all possible tasks.

Model	Tasks	$\mathcal{L}_{CE}^{LCA}$	$y^{LCA} = 0$	$y^{LCA} = 1$	$y^{LCA} = 2$	$y^{LCA} = 3$
GNN	$\mathcal{L}_{CE}^{LCA}$	0.56	$98.220 \pm 0.001$	$68.0 \pm 0.2$	$55.2 \pm 0.1$	$79.9 \pm 0.2$
GNN	$\mathcal{L}_{CE}^{LCA}, \mathcal{L}_{BCE}^{prune}$	0.49	$99.441 \pm 0.001$	$75.5 \pm 0.2$	$60.3 \pm 0.1$	$83.2 \pm 0.2$
WGNN	$\mathcal{L}_{CE}^{LCA}$	0.60	$97.955 \pm 0.001$	$63.2 \pm 0.2$	$53.5 \pm 0.1$	$76.1 \pm 0.3$
WGNN	$\mathcal{L}_{CE}^{LCA}, \mathcal{L}_{BCE}^{prune}$	0.47	$99.282 \pm 0.001$	$76.9 \pm 0.2$	$57.9 \pm 0.1$	$85.6 \pm 0.2$
HGNN	$\mathcal{L}_{CE}^{LCA}$	0.54	$98.826 \pm 0.001$	$71.3 \pm 0.2$	$51.6 \pm 0.1$	$80.9 \pm 0.2$
HGNN	$\mathcal{L}_{CE}^{LCA}, \mathcal{L}_{BCE}^{PV}$	0.53	$98.870 \pm 0.001$	$71.8 \pm 0.2$	$52.7 \pm 0.1$	$82.5 \pm 0.2$
HGNN	$\mathcal{L}_{CE}^{LCA}, \mathcal{L}_{BCE}^{PV}, \mathcal{L}_{BCE}^{prune}$	0.49	$99.289 \pm 0.001$	$75.8 \pm 0.2$	$61.4 \pm 0.1$	$83.9 \pm 0.2$
WHGNN	$\mathcal{L}_{CE}^{LCA}$	0.58	$98.683 \pm 0.001$	$68.5 \pm 0.2$	$52.8 \pm 0.1$	$76.7 \pm 0.2$
WHGNN	$\mathcal{L}_{CE}^{LCA}, \mathcal{L}_{BCE}^{PV}$	0.51	$98.959 \pm 0.001$	$71.7 \pm 0.2$	$54.8 \pm 0.1$	$83.2 \pm 0.2$
WHGNN	$\mathcal{L}_{CE}^{LCA}, \mathcal{L}_{BCE}^{PV}, \mathcal{L}_{BCE}^{prune}$	0.46	$99.274 \pm 0.001$	$75.9 \pm 0.2$	$61.3 \pm 0.1$	$84.0 \pm 0.2$

**Table 1.** Comparison of the LCAG loss value and class accuracies in percent on the test dataset for various architectural ablations. The uncertainties on the LCAG class accuracies are statistical in nature.

#### 4.2. Pruning performance

Figure 2(a-b) shows the discrimination power of the track edge and node scores  $\hat{y}^{etr}$  and  $\hat{y}^{vtr}$  at HGNN layers 1, 2, 3 and 8. The discrimination power increases significantly between layer 1 and 2 particularly for the edges, with the area under curve (AUC) increasing from 0.973 to 0.999. While the discrimination power saturates with subsequent layers, there are marginal increases in discrimination power with each HGNN layer.

Figure 2(c) and (d) further quantify the performance of the pruning after having applied a selection for the LCAG class prediction to be above zero. In particular, Figure 2(c) displays the relationship between the number of tracks from beauty hadrons and the number of tracks selected with a tight pruning selection,  $\hat{y}_8^{etr} > 0.2$  and  $\hat{y}_8^{vtr} > 0.2$ . Meanwhile, Figure 2(d) compares the efficiencies on signal and background tracks, as a function of track multiplicity for the tight pruning selection and a looser pruning selection with  $\hat{y}_8^{etr} > 0.01$  and  $\hat{y}_8^{vtr} > 0.01$ . The efficiencies are defined by the ratio of surviving signal and background tracks after the pruning and LCAG selections.

Node and edge pruning layers aim to accelerate the inference time of the models, particularly the scaling of inference time with track multiplicity. Figure 3 shows GPU and single-threaded CPU inference times, measured with a NVIDIA RTX 4090 GPU and a Intel Core i9-14900K 3.2 GHz CPU, as a function of track multiplicity for the cases of no pruning selection and a loose edge pruning selection at layers 1-3 ( $\hat{y}_{1-3}^{etr/vtr} > 10^{-4}$ ). Early edge pruning yields noticeable speed-ups above roughly 250 tracks; at multiplicities exceeding 400, we observe a 2-3 $\times$  acceleration on GPU and a 5 $\times$  acceleration on CPU. For example, at around 300 tracks, single-threaded CPU inference with early pruning takes about 300 ms compared to the 2.2 s timing reported for the multi-stage GNN approach in DFEI [22] on a 2.2 GHz Intel Core processor. Appendix C presents analogous results for batches of eight events.

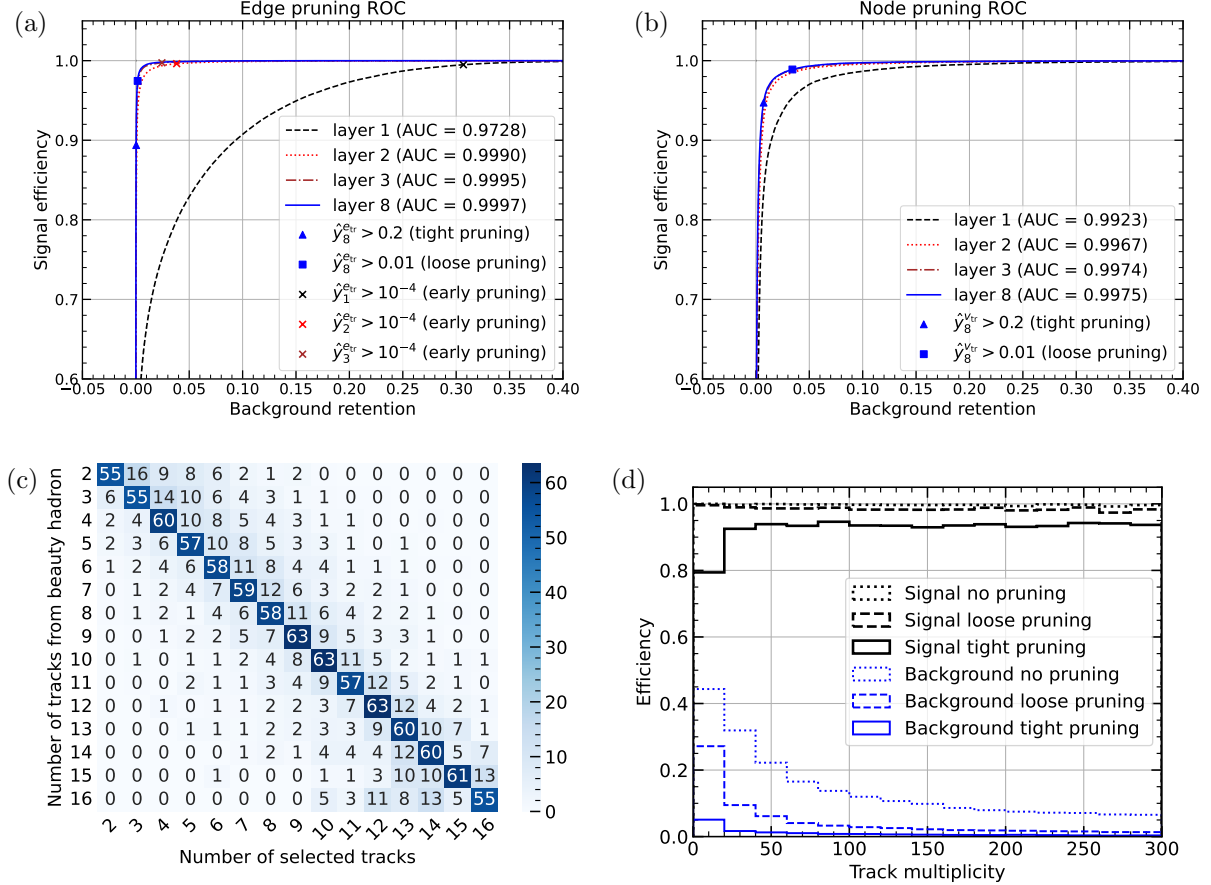


**Figure 2.** (a) and (b) Receiver Operating Characteristic curves for edge and node scores  $\hat{y}^{e_{tr}}$  and  $\hat{y}^{v_{tr}}$  at layers 1, 2, 3 and 8. Pruning selections used by subsequent results are highlighted. (c) Relationship between the number of particles from a beauty hadron and the number of particles selected with a tight edge and node pruning  $\hat{y}_8^{e_{tr}} > 0.2$  and  $\hat{y}_8^{v_{tr}} > 0.2$ . (d) Signal efficiency and background retention as a function of track multiplicity for tight and loose ( $\hat{y}_8^{e_{tr}} > 0.01$  and  $\hat{y}_8^{v_{tr}} > 0.01$ ) pruning selections.

#### 4.3. Reconstruction performance

The beauty hadron reconstruction performance is assessed by categorising reconstructed beauty decay chains into several types introduced in [22]: perfect reconstruction (the reconstructed decay products and the decay hierarchy are both correct and there are no missing decay products, as shown in Figure 1); complete reconstruction (all decay products are correct with none missing; however, the hierarchy is incorrect); not isolated reconstruction (in the reconstruction there are one or more decay products, which are not correct); and partial reconstruction (there are missing decay products). For reconstruction performance we require that the predicted LCAG class is above zero and employ the tight pruning selection,  $\hat{y}_8^{e_{tr}} > 0.2$  and  $\hat{y}_8^{v_{tr}} > 0.2$  introduced in section 4.2.

Table 4.3 compares the reconstruction performance of the DFEI with the proposed GNN and HGNN models for inclusive beauty hadron collision events. All models significantly outperform the DFEI based on the percentage of perfect hierarchy and complete reconstruction with a much lower occurrence of not isolated decays and a similar level of partial reconstruction.

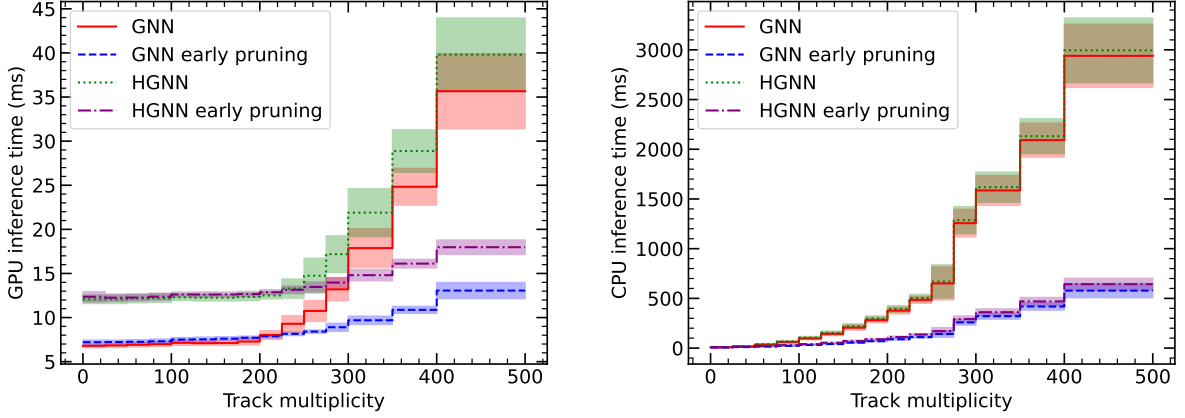


**Figure 3.** GNN and HGNN GPU and CPU mean inference time as a function of track multiplicity per event with and without early pruning ( $\hat{y}_{1-3}^{e_{tr}/v_{tr}} > 10^{-4}$ ). The error bands indicate  $\pm 1\sigma$ , where  $\sigma$  is the standard deviation of the inference time.

For instance, the HGNN architecture, which slightly outperforms the other models, has a perfect reconstruction 4.8 times that of the DFEI.

Model	Perfect reco.	Complete reco.	Not isolated	Part. reco.
DFEI	$4.7 \pm 0.2$	$6.1 \pm 0.2$	$76.1 \pm 0.4$	$13.1 \pm 0.3$
GNN	$21.6 \pm 0.4$	$20.8 \pm 0.4$	$43.8 \pm 0.4$	$13.8 \pm 0.3$
WGNN	$20.9 \pm 0.4$	$20.0 \pm 0.4$	$44.9 \pm 0.4$	$14.2 \pm 0.3$
HGNN	$22.4 \pm 0.4$	$20.1 \pm 0.4$	$44.1 \pm 0.4$	$13.4 \pm 0.3$
WHGNN	$21.5 \pm 0.4$	$19.3 \pm 0.3$	$45.8 \pm 0.4$	$13.5 \pm 0.3$

**Table 2.** Comparison of the percentage of each reconstruction category in 10,000 inclusive beauty hadron events using the DFEI method and the GNN/HGNN architectures with tight last layer pruning. Errors show the corresponding statistical uncertainty.

When early pruning is used to accelerate the inference time, there can be a significant drop in performance if pruning cuts are too tight. This is illustrated in Figure 4, which shows the trade-off between reconstruction performance and GPU inference time for track multiplicities above 300 for HGNN and WHGNN models. A gradual tightening of pruning selections in layers 1-3 are applied ranging from  $\hat{y}_{1-3}^{e_{tr}} > 10^{-7}$  to  $\hat{y}_{1-3}^{e_{tr}} > 10^{-2}$  in multiples of 10. The WHGNN exhibits a greater invariance of performance with pruning, which allows for smaller inference times at minimal reconstruction performance loss.

The reconstruction performance can be further quantified on several exclusive beauty hadron decays with different decay topologies. Table 3 compares the performance of the DFEI model (DF) and the HGNN architecture (H1) on a variety of specific decay modes. While the HGNN often outperforms the DFEI in terms of perfect and complete reconstruction categories and has a smaller fraction of not isolated reconstruction, it suffers from larger levels of partial reconstruction. For comparison, an equivalent HGNN (H2) was trained with the addition of 3000 training samples split uniformly between the decay modes shown in the upper half of Table 3. H2 achieves a much higher perfect hierarchy percentage, while maintaining 1-2% level

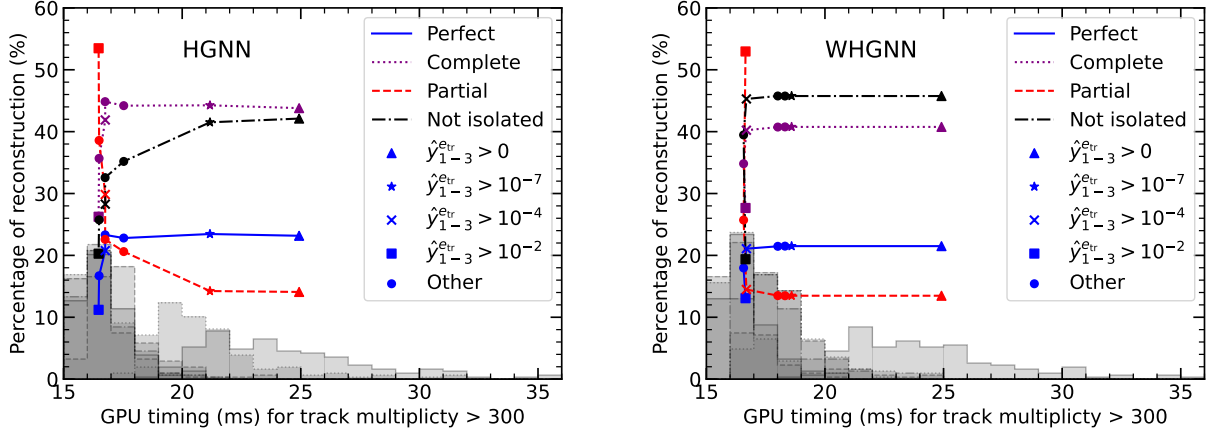


**Figure 4.** Trade off between average GPU timing (ms) and HGNN/WHGNN reconstruction performance for track multiplicity above 300 with no early pruning (the points with the highest GPU timing) and edge pruning in layers 1-3 for selections ranging from  $\hat{y}_{1-3}^{etr} > 10^{-7}$  to  $\hat{y}_{1-3}^{etr} > 10^{-2}$  in multiples of 10. Shaded histograms of the timing distribution are indicated below.

of partial reconstruction. Moreover, H2 generalises to similar exclusive decays not seen during training, as demonstrated in the lower half of Table 3.

Decay	Perfect reco.			Complete reco.			Not isolated			Part reco.		
	DF	H1	H2	DF	H1	H2	DF	H1	H2	DF	H1	H2
inclusive beauty	4.7	22.4	21.9	6.1	20.1	20.6	76.1	44.1	44.1	13.1	13.4	13.4
$B^0 \rightarrow K^{*0} \mu \mu$	32.7	20.3	92.4	17.8	37.7	1.1	43.9	6.2	4.7	5.6	35.8	1.8
$B^0 \rightarrow K \pi$	38.1	47.4	91.6	0.0	0.0	0.0	54.7	10.2	7.0	7.2	42.4	1.4
$B^+ \rightarrow K \pi \pi$	35.6	23.7	94.5	10.3	26.3	0.2	46.5	8.5	4.7	7.6	41.5	0.6
$B_s^0 \rightarrow J/\psi \phi$	31.3	22.8	91.8	20.3	44.3	1.7	44.3	9.9	5.0	4.1	22.9	1.5
$\Lambda_b \rightarrow \Lambda_c^+ \pi$	22.2	27.5	68.3	8.6	9.4	24.4	37.4	7.3	5.2	31.8	55.7	2.1
$B^0 \rightarrow K \mu \mu$	36.2	21.0	93.5	10.4	28.1	0.3	45.9	8.4	4.9	7.5	42.5	1.2
$B_s^0 \rightarrow D_s^- \pi$	33.0	57.7	67.5	7.1	11.6	23.0	53.5	13.1	7.0	6.4	17.6	2.6
$B^0 \rightarrow D^+ D^-$	26.2	37.1	56.7	23.9	40.2	32.1	45.7	14.3	7.3	4.1	8.4	4.0
$\Lambda_b \rightarrow p K$	39.5	24.2	92.3	0.0	0.0	0.0	48.6	5.7	6.4	12.0	70.1	1.3
$\Lambda_b \rightarrow p K \mu \mu$	40.9	11.5	94.7	11.1	17.7	0.5	37.4	4.8	3.7	10.6	66.1	1.1

**Table 3.** Comparison of the beauty hadron reconstruction performance for DFEI and two HGNN models (H1 and H2) with tight pruning, on several exclusive beauty hadron decays. H1 was trained only on inclusive beauty hadron decays while the training of H2 includes a sample of 3000 events split between the decays in the top half the table. We consider the following subdecays  $D^+[K\pi\pi]$ ,  $D_s^-[KK\pi]$ ,  $J/\psi[\mu\mu]$ ,  $\phi[KK]$ ,  $K^{*0}[K\pi]$  and  $\Lambda_c^+[pK\pi]$ .

An example of the HGNN reconstruction is shown in Figure 4.3 for an event with seven PVs with one producing  $B^0 \rightarrow D^+[K^+\pi^+\pi^-]D^-[K^-\pi^+\pi^-]$  and  $B_s^0 \rightarrow \bar{p}\pi^+\pi^+\pi^-(\Lambda \rightarrow p\pi^-)$  decays. Through a combination of integrated pruning and LCAG inference the HGNN is able to isolate the beauty hadron tracks in green and correctly reconstruct the hierarchy of both

decay chains.

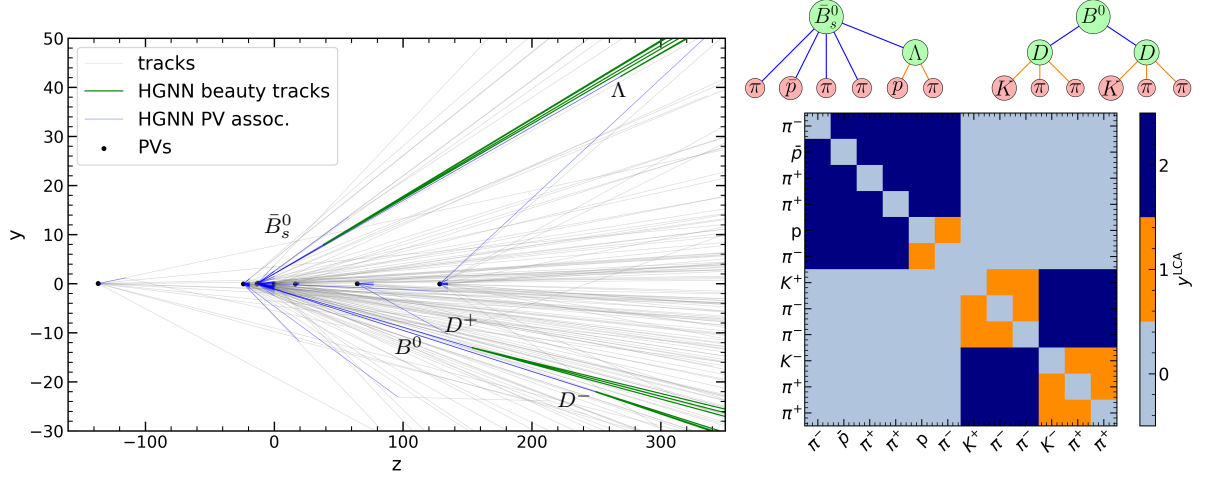


**Figure 5.** Demonstration of the HGNN inference in an event with seven PVs. The HGNN is able to simultaneously associate all tracks to a PV (in blue), isolate the tracks from beauty hadrons via edge and node pruning (in green) and determine the decay hierarchy of both beauty hadrons via its LCAG prediction shown on the right in matrix form.

#### 4.4. PV association

A key additional capability of the HGNN is PV association, which is indicated in the collision event in Figure 4.3 by the blue connections between tracks and PVs. This is most valuable for displaced tracks such as those arising from beauty hadron decays and other long-lived particles. Therefore, we quantify the PV-association for all tracks in the event, tracks from the decays of beauty hadrons and the PV-association of whole beauty hadrons. As discussed in section 3.3, a given track is associated to a PV by selecting the PV-track edge for that track with the highest last layer probability score,  $\hat{y}_8^{e_{pv-tr}}$ . Meanwhile, when evaluating the PV-association of the HGNN for beauty hadrons we use the ground-truth to identify the beauty hadron tracks and associate the beauty hadron to the PV to which the majority of its tracks are associated.

Method			PV Association (%)		
method	task	edge type	track	beauty track	beauty hadron
min IP	-	-	$95.56 \pm 0.03$	$88.82 \pm 0.21$	$96.14 \pm 0.17$
HGNN	$\mathcal{L}_{BCE}^{PV}$	tr-pv	$97.83 \pm 0.02$	$96.19 \pm 0.14$	$97.60 \pm 0.15$
HGNN	$\mathcal{L}_{BCE}^{PV}$	tr-pv, tr-tr	$99.83 \pm 0.01$	$99.74 \pm 0.04$	$99.85 \pm 0.04$
HGNN	$\mathcal{L}_{CE}^{LCA}, \mathcal{L}_{BCE}^{PV}, \mathcal{L}_{BCE}^{prune}$	tr-pv, tr-tr	$99.88 \pm 0.01$	$99.78 \pm 0.04$	$99.85 \pm 0.04$

**Table 4.** Comparison of the average PV association (%) in inclusive beauty hadron events for various HGNN models with more traditional approaches including association with min IP and a MLP.

Table 4.4 reports the average PV association accuracy for the conventional “min IP” method, which assigns each track or beauty hadron to the PV with the smallest impact

parameter, alongside several HGNN variants, distinguished by their training objectives and edge definitions. Figure 6 illustrates how each method’s track-to-PV association performance varies with the number of reconstructed PVs. Across all scenarios, the HGNN models markedly surpass the min IP baseline, achieving up to 99.8% association accuracy for tracks originating from beauty hadrons when track-track edges are incorporated. A similar figure for beauty hadrons is shown in Appendix D.

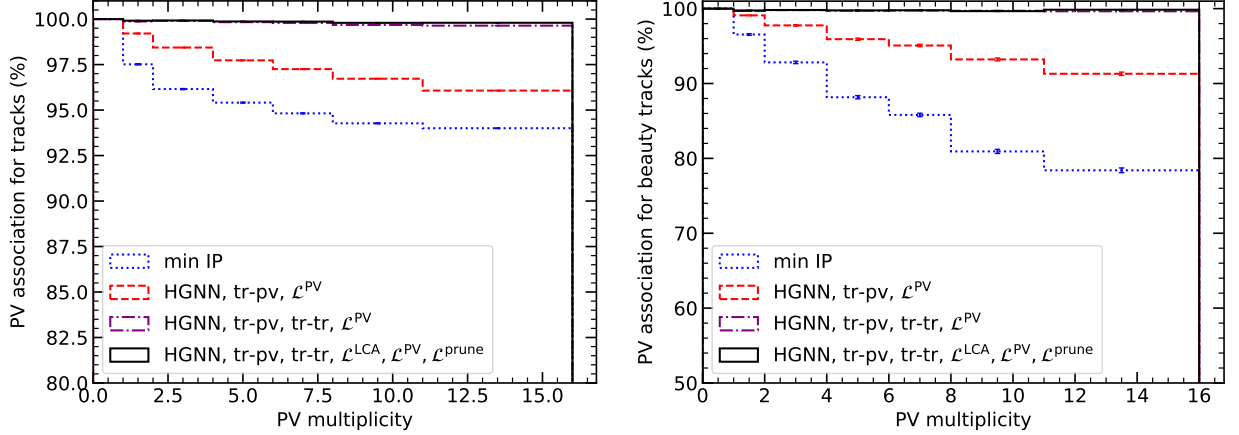


**Figure 6.** Dependence of the average track-to-PV association (%) on PV multiplicity for various methods.

## 5. Discussion

The ablation studies in Section 4.1 demonstrate that the inclusion of additional learning objectives noticeably increases the accuracy on the underlying LCAG reconstruction task. This is especially the case for the pruning task as a high discrimination between signal and background nodes is essential for a correct LCAG reconstruction. Having both track edge and node pruning targets at each layer provides important information, helping models learn richer representations that better discriminate between background and signal nodes. Although smaller in impact, the PV association task also improves the LCAG accuracy, since the tracks of a given beauty hadron associate to the same PV.

GNN and HGNN architectures with integrated pruning demonstrate substantially improved reconstruction performance over DFEI for inclusive beauty hadron decays. This improvement is driven by effective background isolation achieved via tight pruning selections and improved LCAG classification. While the initial training showed a tendency for the HGNN to prune signal particles in rare exclusive hadronic decays ( $\sim 10^{-5}$  frequency or below [50]), a potential issue for trigger applications, this was effectively addressed. By incorporating a subset of these exclusive decays into the HGNN training process, perfect reconstruction rates exceeding 90% were achieved for these challenging modes, with the improvements generalising to similar decays. This highlights the importance of tailored training data for optimising performance on rare topologies. The resulting overall gains in performance promise a major impact on both data acquisition and offline analysis, enabling highly efficient retention of diverse beauty hadron

decays with minimal background.

Another key outcome for practical application is the acceleration in inference time provided by integrated pruning. This enables faster CPU/GPU processing for high track multiplicities with minimal performance loss, which is essential for the model’s scalability as particle collision multiplicity increases in higher luminosity conditions. Here, the proposed weighted message passing scheme, which uses edge and node probability scores,  $\hat{y}^{e/v}$ , as weights during message passing, allows greater performance invariance when pruning. This can be explained by the learned representations being less dependent on background nodes and edges given their small weighting in message passing.

Although HGNN architectures only deliver a slight gain in beauty hadron reconstruction performance than their GNN counterparts, they provide the extra capability of a precise PV association. The architectural advances proposed in this paper have the potential to significantly enhance PV association performance at LHCb. This improvement would, in turn, lead to greater sensitivity across the LHCb physics program by reducing background contributions and enhancing the resolution of key observables. More accurate PV association would have a particularly strong impact on the precision of measurements involving decays with missing particles, such as neutrinos, by enabling a better determination of the B-hadron flight direction.

## 6. Future work

Building on the successful application of HGNNs to beauty hadron reconstruction, several avenues for future development emerge. A major current limitation is the lack of neutral particles, which are potentially challenging to address, primarily because of their lower reconstruction efficiency and resolution compared to charged particles. Within a HGNN, neutral particles can be represented with their own unique representations and learning tasks, which may help overcome the associated difficulties with their inclusion. For instance, regarding multi-task learning, a curriculum learning approach could be employed in which the model first focuses on easier tasks such as learning the LCAG for charged particles and later shifts its attention to tasks involving neutral particles. Beyond incorporating neutrals, several other tasks may be performed to aid reconstruction such as the reconstruction of secondary decay vertices for track-track edges, flavour tagging of reconstructed beauty hadron decays and particle identification of particle nodes.

Several avenues remain for optimisation. First, we did not conduct a comprehensive joint tuning of architectural and training hyperparameters. Second, the edge and node pruning thresholds at each HGNN layer were fixed rather than individually optimised to balance reconstruction accuracy against inference latency. Third, integrating pruning into the training procedure via a “pruning-aware” strategy could yield additional performance gains. Finally, complementary techniques such as model quantisation and weight sparsification could be applied alongside graph pruning to further accelerate inference.

Our current work used a custom simulation environment from DFEI [22], which mimics the Run 3 environment of LHCb. While the simulation considers several reconstruction effects, which are accounted for through experimentally motivated smearing, its limitations (such as the lack of falsely reconstructed tracks and focus on the vertex detector region) necessitate



independent confirmation of the promising performance results using official LHCb simulation and eventually data. Furthermore, additional studies are required to investigate the HGNN reconstruction performance for the high luminosity conditions of LHCb’s Upgrade II. Although higher particle and PV multiplicities pose significant challenges, timing information can be incorporated into the heterogenous graph representation to retain performance.

## 7. Conclusion

Reconstructing beauty hadron decays amidst the high-luminosity conditions of current and future LHC runs presents formidable challenges, including higher particle multiplicities and the prevalence of overlapping primary vertices (PVs), further compounded by strict latency and storage requirements. To address these issues, we have developed a novel HGNN architecture that jointly prunes background, reconstructs beauty-hadron decays, and associates tracks to PVs. By integrating pruning at every layer and optimising with a multi-objective loss, our HGNN achieves substantially higher beauty-hadron reconstruction efficiency and background rejection than the earlier DFEI multi-stage GNN framework [22], while limiting CPU/GPU inference time as particle multiplicity grows.

Central to our design are unique representations for particle tracks and candidate vertices, enabling the HGNN to learn their mutual relations and to assign each track to its true origin vertex with high accuracy. Early-layer pruning coupled with weighted message passing reduces the graph size with negligible performance loss, bounding inference latency even as particle multiplicity grows. These architectural innovations deliver substantial gains in PV association and beauty reconstruction performance, while moving us closer to the stringent latency and storage requirements at data acquisition.

The potential improvement in PV association and beauty hadron reconstruction, would translate into improved sensitivities of precision measurements across the LHCb physics program, reducing sources of background and improving resolutions of derived quantities. More broadly, the architectural novelties are applicable in several particle physics experiments, where heterogeneous datasets, multi-task reconstruction and the scalability of GNN inference time are common.

## 8. Acknowledgements

W. S. and N. S. have received support from the Swiss National Science Foundation (SNF) under TMAG-2\_209263. J.G.P. is supported by the U.S. National Science Foundation under Grant No. 2411204. We acknowledge support from the Italian national funding agency INFN and CERN.

## Appendix A. Training curves

The multi-task training optimises several objectives losses simultaneously. Figure A1 shows contributions to the overall training and validation loss in from equation 3 for GNN and HGNN trainings with training epochs.

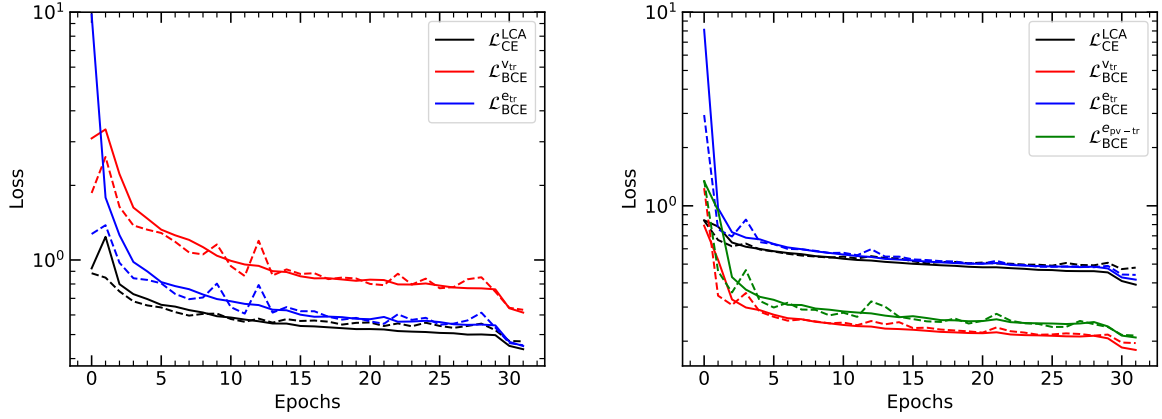


**Figure A1.** Training and validation loss curves with training epochs. The curves are distinguished with solid lines for training and dashed lines for validation.

## Appendix B. Multi-task hyperparameter optimisation

The improvements in performance arising from the multi-task training is dependent on the  $\beta$  parameters which govern the significance of the various tasks. To demonstrate this, we performed a two-dimensional grid scan in  $\beta^{e_{tr}}$  and  $\beta^{v_{tr}}$  as shown in Figure B1, which indicates that the relative significance of the edge and node pruning tasks influence the final  $\mathcal{L}_{CE}^{LCA}$  value.

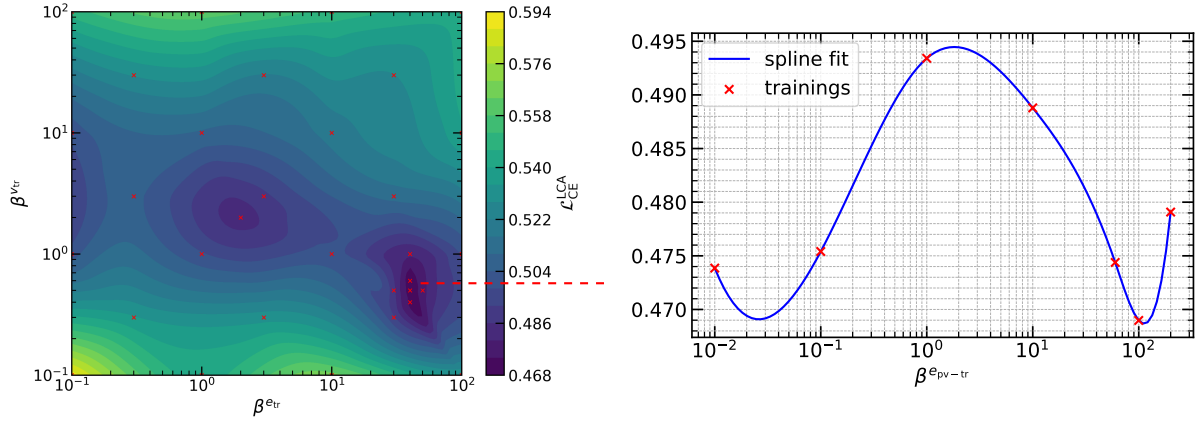


**Figure B1.** Grid scan in  $\beta^{e_{tr}}$  and  $\beta^{v_{tr}}$  showing the final LCA reconstruction loss value,  $\mathcal{L}_{CE}^{LCA}$ . At the approximate position of the minima,  $(\beta^{e_{tr}}, \beta^{v_{tr}}) = (40, 0.6)$ , a one-dimensional scan in  $\beta^{e_{pv-tr}}$  is shown.

Each training is performed in a similar manner to the procedure described in Section 4.1. A global minimum is found approximately in the region  $(\beta^{e_{tr}}, \beta^{v_{tr}}) = (40, 0.6)$ , which indicates that a relatively high weighting of the edge pruning task benefits the LCAG reconstruction task.

## Appendix C. Batch timing

Further accelerations in model inference time are possible by coupling batch inference with early layer pruning. Figure C1 shows the average inference time per event when processing batches of 8 events as a function of the average track multiplicity within the batch.

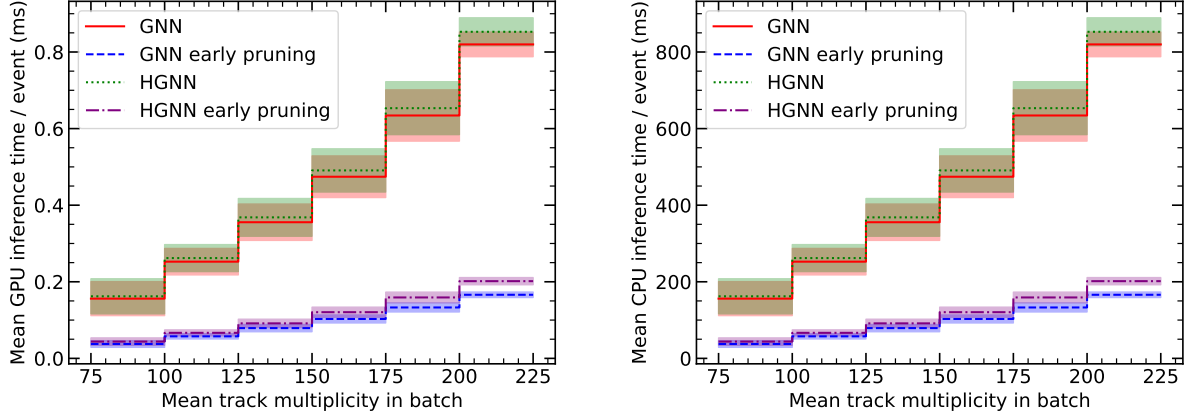


**Figure C1.** Mean GPU and CPU inference time per event with mean track multiplicity for batches of 8 events with and without early pruning ( $\hat{y}_{1-3}^{e_{tr}/v_{tr}} > 10^{-4}$ ).

## Appendix D. PV association

Figure D1 compares the dependence of PV-association for beauty hadrons between the minimum impact parameter method and approaches using HGNNs.

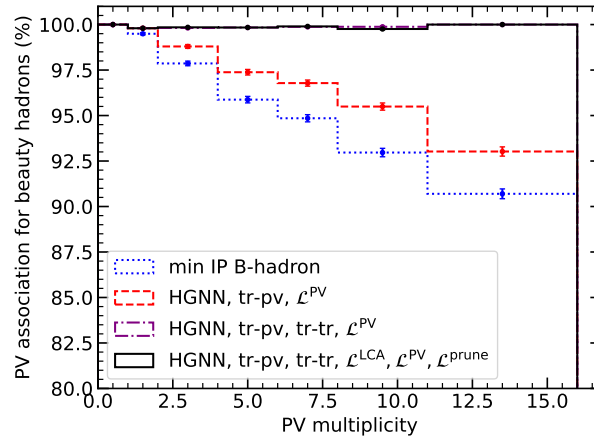


**Figure D1.** Dependence of the average PV association (%) for beauty hadrons between various methods.

## References

- [1] Krizhevsky A, Sutskever I and Hinton G E 2012 Imagenet classification with deep convolutional neural networks *Advances in Neural Information Processing Systems* vol 25 (Curran Associates, Inc.)
- [2] Vaswani A, Shazeer N, Parmar N, Uszkoreit J, Jones L, Gomez A N, Kaiser L and Polosukhin I 2017 Attention is all you need (arXiv1706.03762)
- [3] Wu Z, Pan S, Chen F, Long G, Zhang C and Yu P S 2019 A comprehensive survey on graph neural networks (arXiv1901.00596)
- [4] Yang X, Yan M, Pan S, Ye X and Fan D 2023 Simple and efficient heterogeneous graph neural network (arXiv2207.02547)
- [5] Shi J, Ji H, Shi C, Wang X, Zhang Z and Zhou J 2020 Heterogeneous graph neural network for recommendation (arXiv2009.00799)
- [6] Zhang K, Huang F, Liu L, Xiong Z, Zhang H, Quan Y and Zhang W 2024 Heterogeneous causal metapath graph neural network for gene-microbe-disease association prediction (arXiv2406.19156)
- [7] Wang Z, Liu X, Yang P, Liu S and Wang Z 2021 Cross-lingual text classification with heterogeneous graph neural network *Proceedings of the 59th Annual Meeting of the Association for Computational Linguistics and the 11th International Joint Conference on Natural Language Processing (Volume 2: Short Papers)* pp 612–620
- [8] Crawshaw M 2020 Multi-task learning with deep neural networks: A survey (arXiv2009.09796)
- [9] Radovic A, Williams M, Rousseau D, Kagan M, Bonacorsi D, Himmel A, Aurisano A, Terao K and Wongjirad T 2018 *Nature* **560** 41–48
- [10] Bourilkov D 2020 *Int. J. Mod. Phys. A* **34** 1930019
- [11] Shlomi J, Battaglia P and Vlimant J R 2020 Graph Neural Networks in Particle Physics (arXiv2007.13681)
- [12] Huang A, Ju X, Lyons J, Murnane D, Pettee M and Reed L 2023 *JINST* **18** P07001
- [13] Caillou S, Collard C, Rougier C, Stark J, Torres H and Vallier A 2024 *EPJ Web Conf.* **295** 09028
- [14] Alves Jr A A *et al.* (LHCb) 2008 *JINST* **3** S08005
- [15] Aaij R *et al.* (LHCb) 2024 *JINST* **19** P05065
- [16] Aaij R *et al.* (LHCb) 2018 Physics case for an LHCb Upgrade II - Opportunities in flavour physics, and beyond, in the HL-LHC era
- [17] Aaij R *et al.* 2019 *JINST* **14** P04006
- [18] Aaij R *et al.* (LHCb) 2019 *JINST* **14** P04013
- [19] Aaij R *et al.* (LHCb) 2012 *Phys. Rev. Lett.* **108** 101803
- [20] Aaij R *et al.* (LHCb) 2015 *Nature Physics* **11** 743–747
- [21] Aaij R *et al.* (LHCb) 2025 *Phys. Rev. Lett.* **134** 061801
- [22] García Pardinás J, Calvi M, Eschle J, Mauri A, Meloni S, Mozzanica M and Serra N 2023 *Comput. Softw. Big Sci.* **7** 12
- [23] Gligorov V V and Williams M 2013 *JINST* **8** P02013
- [24] Schulte N, Delaney B R, Nolte N, Ciezarek G M, Albrecht J and Williams M 2023 Development of the Topological Trigger for LHCb Run 3 (arXiv2306.09873)
- [25] Keck T *et al.* 2019 *Comput. Softw. Big Sci.* **3** 6
- [26] Kahn J *et al.* 2022 *Mach. Learn. Sci. Tech.* **3** 035012
- [27] Abumusabih M, Cerasoli J, Dujany G and Santos C 2025 (arXiv2503.09401)
- [28] Elabd A *et al.* 2022 *Front. Big Data* **5** 828666
- [29] Adachi I *et al.* (Belle II) 2024 *Phys. Rev. D* **110** 012001
- [30] Qu H and Gouskos L 2020 *Phys. Rev. D* **101** 056019
- [31] ATLAS 2022 Graph Neural Network Jet Flavour Tagging with the ATLAS Detector ATL-PHYS-PUB-2022-027
- [32] Guo J, Li J, Li T and Zhang R 2021 *Phys. Rev. D* **103** 116025
- [33] Pata J, Duarte J, Vlimant J R, Pierini M and Spiropulu M 2021 *Eur. Phys. J. C* **81** 381
- [34] Ju X *et al.* (Exa.TrkX) 2021 *Eur. Phys. J. C* **81** 876
- [35] Liu R, Calafiura P, Farrell S, Ju X, Murnane D T and Pham T M 2023 Hierarchical Graph Neural Networks for Particle Track Reconstruction *21th International Workshop on Advanced Computing and Analysis Techniques in Physics Research: AI meets Reality* (arXiv2303.01640)
- [36] Qasim S R, Kieseler J, Iiyama Y and Pierini M 2019 *Eur. Phys. J. C* **79** 608

- [37] Birk J, Hallin A and Kasieczka G 2024 *Mach. Learn. Sci. Tech.* **5** 035031
- [38] Golling T, Heinrich L, Kagan M, Klein S, Leigh M, Osadchy M and Raine J A 2024 *Mach. Learn. Sci. Tech.* **5** 035074
- [39] Mikuni V and Nachman B 2025 *Phys. Rev. D* **111** 054015
- [40] Aurisano A, Hewes V, Cerati G, Kowalkowski J, Lee C S, Liao W, Grzenda D, Gumpula K and Zhang X 2024 *Phys. Rev. D* **110** 032008
- [41] Zheng G, Yang Z Y, Liu S, Ma R, Gong X, Wang A, Wang S and Zhong W 2024 *Nuclear Fusion* **64**
- [42] Kipf T N and Welling M 2017 Semi-supervised classification with graph convolutional networks *International Conference on Learning Representations (ICLR)*
- [43] Veličković P, Cucurull G, Casanova A, Romero A, Lio P and Bengio Y 2018 Graph attention networks *International Conference on Learning Representations (ICLR)*
- [44] Gilmer J, Schoenholz S S, Riley P F, Vinyals O and Dahl G E 2017 Neural message passing for quantum chemistry *Advances in Neural Information Processing Systems* vol 30 pp 129–139
- [45] Battaglia P W *et al.* 2018 Relational inductive biases, deep learning, and graph networks (arXiv1806.01261)
- [46] Li Q, Han Z and Wu X 2018 Deeper insights into graph convolutional networks for semi-supervised learning *AAAI Conference on Artificial Intelligence (AAAI)* p 3538–3545
- [47] García Pardinás J, Calvi M, Eschle J, Mauri A, Meloni S, Mozzanica M and Serra N 2023 Dataset of paper “GNN for Deep Full Event Interpretation and hierarchical reconstruction of heavy-hadron decays in proton-proton collisions” URL <https://doi.org/10.5281/zenodo.7799170>
- [48] Bierlich C *et al.* 2022 A comprehensive guide to the physics and usage of PYTHIA 8.3 (arXiv2203.11601)
- [49] Ryd A, Lange D, Kuznetsova N, Versille S, Rotondo M, Kirkby D P, Wuerthwein F K and Ishikawa A 2005 EvtGen: A Monte Carlo Generator for B-Physics
- [50] Navas S *et al.* (Particle Data Group) 2024 *Phys. Rev. D* **110** 030001